Research Article | Vol. 7, No. 6 | 1 Jun 2017 | OPTICAL MATERIALS EXPRESS 2030

Optical Materials EXPRESS

Orientation-dependent electro-optical response of $BaTiO_3$ on $SrTiO_3$-buffered Si(001) studied via spectroscopic ellipsometry

Min-Hsiang Mark Hsu,[1,2,*] Antonio Marinelli,[3] Clement Merckling,[1] Marianna Pantouvaki,[1] Joris Van Campenhout,[1] Philippe Absil,[1] and Dries Van Thourhout[2,4]

[1]*imec, Kapeldreef 75, 3001, Leuven, Belgium*
[2]*Photonics Research Group, INTEC, Ghent University –imec, Ghent, 9000 Belgium*
[3]*Dipartimento di Elettronica e Telecomunicazioni, Politecnico Di Torino, Corso Duca Degli Abruzzi, Torino, 4-70126 Italy*
[4]*Center for Nano- and Biophotonics (NB-Photonics), Ghent University, Ghent, 9000 Belgium*
**min.hsiang.hsu@imec.be*

Abstract: To design a high performance $BaTiO_3$ (BTO)-integrated Si modulator, understanding how BTO domain orientations influence its electro-optical (EO) properties is crucial. The 100-nm-thick BTO films with c-oriented and a-oriented domains are obtained by exploiting various thickness of $SrTiO_3$ buffer layers grown on Si(001) substrates. Then, the electro-optical behavior for 2 differently oriented samples is analyzed using spectroscopic ellipsometry.

OCIS codes: (160.2660) Ferroelectrics; (160.2100) Electro-optical materials; (190.4400) Nonlinear optics, materials; (310.0310) Thin films; (310.3840) Materials and process characterization; (310.6860) Thin films, optical properties.

References and links

1. E. Bousquet, M. Dawber, N. Stucki, C. Lichtensteiger, P. Hermet, S. Gariglio, J. M. Triscone, and P. Ghosez, "Improper ferroelectricity in perovskite oxide artificial superlattices," Nature **452**(7188), 732–736 (2008).
2. C. C. Homes, T. Vogt, S. M. Shapiro, S. Wakimoto, and A. P. Ramirez, "Optical response of high-dielectric-constant perovskite-related oxide," Science **293**(5530), 673–676 (2001).
3. R. W. Whatmore, "Pyroelectric ceramics and devices for thermal infra-red detection and imaging," Ferroelectrics **118**(1), 241–259 (1991).
4. Y. Saito, H. Takao, T. Tani, T. Nonoyama, K. Takatori, T. Homma, T. Nagaya, and M. Nakamura, "Lead-free piezoceramics," Nature **432**(7013), 84–87 (2004).
5. F. S. Chen, J. E. Geusic, S. K. Kurtz, J. G. Skinner, and S. H. Wemple, "Light Modulation and Beam Deflection with Potassium Tantalate-Niobate Crystals," J. Appl. Phys. **37**(1), 388–398 (1966).
6. B. W. Wessels, "Ferroelectric Epitaxial Thin Films for Integrated Optics," Annu. Rev. Mater. Res. **37**(1), 659–679 (2007).
7. E. L. Wooten, K. M. Kissa, A. Yi-Yan, E. J. Murphy, D. A. Lafaw, P. F. Hallemeier, D. Maack, D. V. Attanasio, D. J. Fritz, G. J. McBrien, and D. E. Bossi, "A review of lithium niobate modulator for fiber-optic communications systems," IEEE J. Sel. Top. Quantum Electron. **6**(1), 69–82 (2000).
8. L. Arizmendi, "Photonic applications of lithium niobate crystals," Phys. Status Solidi **201**(2), 253–283 (2004).
9. R. A. Soref and B. R. Bennett, "Electrooptical effect in silicon," IEEE J. Quantum Electron. **23**(1), 123–129 (1987).
10. A. Liu, R. Jones, L. Liao, D. Samara-Rubio, D. Rubin, O. Cohen, R. Nicolaescu, and M. Paniccia, "A high-speed silicon optical modulator based on a metal-oxide-semiconductor capacitor," Nature **427**(6975), 615–618 (2004).
11. M. Pantouvaki, P. Verheyen, J. D. Coster, G. Lepage, P. Absil, and J. V. Campenhout, "56Gb/s ring modulator on a 300mm silicon photonics platform," in 2015 European Conference on Optical Communication (ECOC), 2015), 1–3.
12. G. T. Reed and C. E. Jason Png, "Silicon optical modulators," Mater. Today **8**(1), 40–50 (2005).
13. R. S. Jacobsen, K. N. Andersen, P. I. Borel, J. Fage-Pedersen, L. H. Frandsen, O. Hansen, M. Kristensen, A. V. Lavrinenko, G. Moulin, H. Ou, C. Peucheret, B. Zsigri, and A. Bjarklev, "Strained silicon as a new electro-optic material," Nature **441**(7090), 199–202 (2006).
14. P. Rabiei, J. Ma, S. Khan, J. Chiles, and S. Fathpour, "Heterogeneous lithium niobate photonics on silicon substrates," Opt. Express **21**(21), 25573–25581 (2013).
15. A. Yariv and P. Yeh, *Optical Waves in Crystals* (Wiley, 1984), Vol. 10.
16. A. A. Demkov and A. B. Posadas, *Integration of Functional Oxides with Semiconductors* (Springer, 2014).

#291887 https://doi.org/10.1364/OME.7.002030
Journal © 2017 Received 31 Mar 2017; revised 14 May 2017; accepted 15 May 2017; published 19 May 2017
Corrected: 19 June 2017

Optical Materials EXPRESS

17. J. W. Reiner, A. M. Kolpak, Y. Segal, K. F. Garrity, S. Ismail-Beigi, C. H. Ahn, and F. J. Walker, "Crystalline oxides on silicon," Adv. Mater. **22**(26-27), 2919–2938 (2010).
18. D. G. Schlom, L.-Q. Chen, X. Pan, A. Schmehl, and M. A. Zurbuchen, "A Thin Film Approach to Engineering Functionality into Oxides," J. Am. Ceram. Soc. **91**(8), 2429–2454 (2008).
19. R. McKee, F. Walker, and M. Chisholm, "Crystalline oxides on silicon: the first five monolayers," Phys. Rev. Lett. **81**(14), 3014–3017 (1998).
20. C. Xiong, W. H. Pernice, J. H. Ngai, J. W. Reiner, D. Kumah, F. J. Walker, C. H. Ahn, and H. X. Tang, "Active silicon integrated nanophotonics: ferroelectric $BaTiO_3$ devices," Nano Lett. **14**(3), 1419–1425 (2014).
21. S. Abel, T. Stoferle, C. Marchiori, D. Caimi, L. Czornomaz, M. Stuckelberger, M. Sousa, B. J. Offrein, and J. Fompeyrine, "A Hybrid Barium Titanate–Silicon Photonics Platform for Ultraefficient Electro-Optic Tuning," J. Lightwave Technol. **34**(8), 1688–1693 (2016).
22. K. J. Choi, M. Biegalski, Y. L. Li, A. Sharan, J. Schubert, R. Uecker, P. Reiche, Y. B. Chen, X. Q. Pan, V. Gopalan, L. Q. Chen, D. G. Schlom, and C. B. Eom, "Enhancement of ferroelectricity in strained BaTiO3 thin films," Science **306**(5698), 1005–1009 (2004).
23. C. Dubourdieu, J. Bruley, T. M. Arruda, A. Posadas, J. Jordan-Sweet, M. M. Frank, E. Cartier, D. J. Frank, S. V. Kalinin, A. A. Demkov, and V. Narayanan, "Switching of ferroelectric polarization in epitaxial $BaTiO_3$ films on silicon without a conducting bottom electrode," Nat. Nanotechnol. **8**(10), 748–754 (2013).
24. C. Merckling, G. Saint-Girons, C. Botella, G. Hollinger, M. Heyns, J. Dekoster, and M. Caymax, "Molecular beam epitaxial growth of BaTiO3 single crystal on Ge-on-Si(001) substrates," Appl. Phys. Lett. **98**(9), 092901 (2011).
25. G. Delhaye, C. Merckling, M. El-Kazzi, G. Saint-Girons, M. Gendry, Y. Robach, G. Hollinger, L. Largeau, and G. Patriarche, "Structural properties of epitaxial SrTiO3 thin films grown by molecular beam epitaxy on Si(001)," J. Appl. Phys. **100**(12), 124109 (2006).
26. N. Lucas, H. Zabel, H. Morkoc, and H. Unlu, "Anisotropy of thermal expansion of GaAs on Si(001)," Appl. Phys. Lett. **52**(25), 2117–2119 (1988).
27. M. H. M. Hsu, D. Van Thourhout, M. Pantouvaki, J. Meersschaut, T. Conard, O. Richard, H. Bender, P. Favia, M. Vila, R. Cid, J. Rubio-Zuazo, G. R. Castro, J. Van Campenhout, P. Absil, and C. Merckling, "Controlled orientation of molecular-beam-epitaxial BaTiO3 on Si(001) using thickness engineering of BaTiO3 and SrTiO3 buffer layers," to be published in Appl. Phys. Express.
28. F. Eltes, D. Caimi, F. Fallegger, M. Sousa, E. O'Connor, M. D. Rossell, B. Offrein, J. Fompeyrine, and S. Abel, "Low-loss BaTiO3–Si waveguides for nonlinear integrated photonics," ACS Photonics **3**(9), 1698–1703 (2016).
29. M. Li, J. Zhou, X. Jing, M. Zeng, S. Wu, J. Gao, Z. Zhang, X. Gao, X. Lu, J. M. Liu, and M. Alexe, "Controlling resistance switching polarities of epitaxial BaTiO3 films by mediation of ferroelectricity and oxygen vacancies," Adv. Electron. Mater. **1**(6), 1500069 (2015).
30. M. H. M. Hsu, C. Merckling, S. El Kazzi, M. Pantouvaki, O. Richard, H. Bender, J. Meersschaut, J. Van Campenhout, P. Absil, and D. Van Thourhout, "Diffraction studies for stoichiometry effects in BaTiO3 grown by molecular beam epitaxy on Ge(001)," J. Appl. Phys. **120**(22), 225114 (2016).
31. D. Crandles, B. Nicholas, C. Dreher, C. Homes, A. McConnell, B. Clayman, W. Gong, and J. Greedan, "Optical properties of highly reduced SrTiO 3-x," Phys. Rev. B **59**(20), 12842–12846 (1999).
32. M. H. M. Hsu et al., imec, Kapeldreef 75, 3001, Leuven, Belgium, are preparing a manuscript to be called "Crystal structures and ferroelectricity for epitaxial $BaTiO_3$ on $SrTiO_3$-on-Si pseudo-substrate using plasma-assisted molecular beam epitaxy."
33. D. V. Likhachev, N. Malkova, and L. Poslavsky, "Modified Tauc–Lorentz dispersion model leading to a more accurate representation of absorption features below the bandgap," Thin Solid Films **589**, 844–851 (2015).
34. M. Zgonik, P. Bernasconi, M. Duelli, R. Schlesser, P. Günter, M. H. Garrett, D. Rytz, Y. Zhu, and X. Wu, "Dielectric, elastic, piezoelectric, electro-optic, and elasto-optic tensors of $BaTiO_3$ crystals," Phys. Rev. B Condens. Matter **50**(9), 5941–5949 (1994).

1. Introduction

Owing to their relaxed ionic bonds and transition metal cations, ferroelectric oxides simultaneously possess strong dielectric, piezoelectric, linear electro-optical (EO, also known as the Pockels effect), and pyroelectric behavior [1–6].

Historically, fiber optics telecom systems have exploited the relatively high Pockels coefficient (~30 pm/V) of the ferroelectric material $LiNbO_3$ (LNO) to achieve high performance optical modulators [7,8]. More recently, Si-based photonic integrated circuits have employed carrier dispersion effects to achieve high-speed Si modulators. However, for photonic systems using higher order modulation scheme, such as quadrature phase shift keying, exploiting the carrier dispersion effect leads to sub-optimal performance [7]. Thus, for these applications, it would be more advantageous to employ a pure phase modulator that utilizes the Pockels effect rather than the carrier dispersion effect to avoid unbalanced amplitude modulation. However, as is well known, bulk silicon does not exhibit a linear

Optical Materials EXPRESS

electro-optic effect given its centro-symmetric crystal structure [9–12]. Therefore, several groups have investigated how to break this crystal symmetry in silicon waveguides, e.g. through the deposition of a highly strained silicon nitride layer, resulting in a Pockels coefficient of ~1.7 pm/V [13]. In a different approach, Rabiei et al. used a wafer-bonding technique to transfer a LNO thin film onto a silicon substrate. They demonstrated an EO coefficient of ~30 pm/V, which is comparable to the EO performance of bulk LNO [14]. Among the various ferroelectric oxides, $BaTiO_3$ (BTO) exhibits a much more pronounced Pockels coefficient [6,15] however, at least in bulk crystals. In thin film applications, its EO behavior depends on its crystallinity, with single crystalline BTO displaying the best properties [16–18]. However, it is challenging to integrate high quality crystalline BTO thin films on a Si(001) substrate owing to their largely different crystal structure and chemical properties [16]. The in-plane lattice constant ($a_{//}$) of BTO is 0.3992 nm, while that of silicon is 0.5431 nm; this constitutes a lattice mismatch of 27%. Besides, BTO is chemically unstable when deposited directly on silicon, resulting in the formation of an amorphous silicate layer and inhibiting the synthesis of high-quality epitaxial BTO. This particular problem was not resolved until the late 1990s, when McKee et al. utilized a ½ monolayer (ML) of SrO to obtain a high quality $SrTiO_3$ (STO) layer using molecular beam epitaxy (MBE) [19]. Although bulk STO and Si still have a cubic-to-cubic lattice mismatch of around 28% (STO for $a_{//}$ is 0.3905 nm), a ½ ML of SrO can be used as a lattice template to initiate a 45° rotation of the STO lattice with respect to the Si lattice, reducing the remaining lattice mismatch to 2% (Si/$\sqrt{2}$ = 0.3840 nm). Building further on this development, the chemical rejection between BTO and Si can now be resolved via the insertion of STO, which present similar crystal and chemical structures to BTO [16]. Moreover, the lattice mismatch between BTO and STO is only 2%. Thus, STO can be used to facilitate the monolithic integration of BTO thin films on Si(001) using MBE. Recently, based on this growth technique, the high speed silicon integrated modulators that exploit the excellent EO properties of BTO have been successfully demonstrated. Xiong et al. [20] and Abel et al. [21] presented hybrid BTO/Si optical modulators showing the bandwidth of 5 GHz and effective Pockels coefficient of 300 pm/V respectively.

Nevertheless, the strain owing to the remaining mismatch of the lattice constants and the different thermal expansion coefficients results in multi-domains within the BTO layers grown on STO-buffered Si(001) [22–24]. BTO has a tetragonal crystal structure, with its optical axis along $<100>_{BTO}$, resulting in six possible domain orientations: two 180°-type domains (c-oriented, out-of-plane optical axis) and four 90°-type domains (a-oriented, in-plane optical axis). Given the optical anisotropy of BTO, the EO behavior of a BTO-based modulator will be dependent on the relationship between the BTO domain orientation (i.e. the BTO optical axis), the externally applied electric field, and the polarization of the optical signal [15]. To design a high performance BTO-integrated Si modulator, it is crucial to understand how these mixtures of the domains influence its EO properties.

Therefore, we use spectroscopic ellipsometry (SE) to investigate how the EO response of two differently grown films depends on their respective domain orientation. The 100 nm BTO films are grown using plasma-assisted MBE starting from respectively a 10 nm and a 40 nm STO buffer layer deposited on highly p-doped Si(001) substrates. Via X-ray diffraction (XRD), the BTO film grown on the 10-nm-thick STO buffer is identified as being more a-oriented while the BTO layer grown on 40-nm-thick STO is shown to be more c-oriented. Then, we analyze the EO behavior in a- and c-oriented BTO films by studying the interplay between domain orientations and applied electric field.

2. Experiments

All of the samples were grown on highly p-doped 200mm Si(001) (p^+-Si) substrates in a Riber49 200 mm production MBE reactor. Ti was evaporated with an electron beam that was controlled by a feedback loop from a mass spectrometer to maintain a constant flux during

Optical Materials EXPRESS

growth. A Ba atomic flux was obtained using a standard Knudsen effusion cell and the [Ba]/[Ti] flux ratio was calibrated with the help of a quartz crystal microbalance as well as Rutherford backscattering spectroscopy (RBS). A remote plasma source was used to produce atomic oxygen during the growth.

Prior to STO deposition, 2 ML of Sr was deposited on the substrate at 650 °C. Then the Sr-covered Si substrate was ramped up to 800 °C until a bright 2 × 1 reflection high energy electron diffraction (RHEED) reconstruction pattern was obtained. The substrate was then cooled back to 600 °C. Meanwhile, the RHEED reconstruction pattern evolved to a 2 × 3 pattern, revealing a 1/6 ML of Sr remaining on the surface. Additional Sr was added until a ½ ML of Sr (confirmed by RBS) was obtained, resulting again in a 2 × 1 RHEED pattern. This ½ ML of Sr not only serves as a crystal template to drive the desired 45° lattice rotation of the STO layer with respect to Si(001), but also protects the Si surface from being oxidized. Afterwards, 6 ML (2.4 nm) of STO was deposited at 150 °C under an oxygen partial pressure of ~4×10^{-7} Torr. This layer's RHEED pattern showed that it was amorphous owing to insufficient oxygen and the temperature being too low. Then, the substrate was heated up to 550 °C without oxygen flux for recrystallization until the RHEED lines became sharp and stable. To ensure the initial STO crystallinity, we repeated the above STO deposition steps once more to obtain a 5 nm STO layer on the Si(001) substrate. After the second recrystallization step at 550 °C, the remainder of the STO layer (5nm or 35nm) was grown at the same temperature and under an oxygen partial pressure of ~1.2×10^{-6} Torr until the desired thickness was reached. Then, the substrate temperature was ramped up to 630 °C to grow a 100-nm-thick BTO layer under an oxygen partial pressure of ~1.6×10^{-6} Torr. In the next sections, we present and discuss the detailed crystal, electrical, and optical characteristics of these layers.

3. Results and discussions

3.1 Crystal structures and domain orientations

In this section, the XRD analysis is performed to identify the domain orientation and crystallinity in 100-nm-thick BTO samples on Si(001) substrate using 10 nm and 40 nm STO buffer layers. Figure 1(a) presents ω-2θ XRD scans along $[001]_{BTO}$ and $[101]_{BTO}$. Based on the position of the Bragg peaks along $(002)_{BTO/STO}$ and $(202)_{BTO/STO}$, the average in-plane lattice constant $a_{//}$, the out-of-plane lattice constant $a_{\perp}$, and the tetragonality $a_{\perp}/a_{//}$ of the samples can be extracted. The lattice parameters of bulk BTO can be taken as a reference: bulk c-oriented BTO has $a_{//}$ = 0.3992 nm, $a_{\perp}$ = 0.4036 nm, and tetragonality = 1.011; bulk a-oriented BTO has $a_{//}$ = 0.4036 nm, $a_{\perp}$ = 0.3992 nm, and tetragonality = 0.989. Derived from the data in Fig. 1(a), the $a_{\perp}$, average $a_{//}$ and tetragonality values for the BTO layer grown on the 40-nm-thick STO buffer layer are 0.4022 nm, 0.4003 nm, and 1.005, respectively. The tetragonality greater than unity indicates that domains in this layer are mostly c-oriented. On the other hand, for the BTO layer grown on the 10-nm-thick STO buffer, $a_{\perp}$ = 0.3997 nm, average $a_{//}$ = 0.4039 nm, and $a_{\perp}/a_{//}$ = 0.990 are evaluated, indicating that a-oriented domains are predominant. The different behavior of both samples is driven by the trade-off between the compressive and tensile strain in the BTO/STO/Si(001) heterostructures. The compressive strain resulted from the smaller $a_{//}$ for the underlying STO layer ($a_{//}$ = 0.3905 nm for bulk STO and $a_{//}$ = 0.3992 nm for bulk c-oriented BTO) tends to favor c-oriented BTO. Conversely, because of the difference in the thermal expansion coefficients of Si and BTO ($\alpha_{si} = 2.6 \times 10^{-6}$ K^{-1} for Si and $\alpha_{BTO} = 11 \times 10^{-6}$ K^{-1} for bulk BTO), the tensile strain is also exerted on the BTO layer, favoring a-oriented domains. By using the 10 nm thick STO buffer, the BTO layer is close to the Si surface. When cooling down after the growth, the Si thermal expansion drives the contraction of the BTO in-plane lattice [25,26]. Therefore, the tensile strain is formed, leading the BTO orientation to be more a-oriented [25]. Nevertheless, by using a 40-nm-thick STO buffer layer as a “spacer” between the BTO and Si, the effect from the Si

Optical Materials EXPRESS

thermal expansion coefficient, which brings about the tensile strain, is attenuated. Thus, the compressive strain induced by the difference in lattice constants becomes dominant, facilitating more c-oriented domains in the BTO layer. More details of the thickness engineering to control BTO orientations can be found elsewhere [27]. For convenience, in the remainder of this work, we will denote the samples grown on the 10- and 40-nm-thick STO buffer layer as a-oriented and c-oriented, respectively. Figure 1(b) presents the azimuthal ϕ scan of $(202)_{STO}$, $(202)_{BTO}$ and $(202)_{Si}$ for c-oriented BTO. Due to the 4-fold symmetry, periodicity in the ϕ-scan spectrum is 90°. In addition, the ½ ML of Sr at the interface between STO and Si initiates 45° lattice rotation, making an epitaxial STO buffer layer on Si(001) feasible. Then, the BTO layer can be epitaxially grown onto the STO buffer. Thus, the epitaxial relationship for the BTO/STO/Si(001) stack is as follows: <100>BTO(001)//<100>STO(001)//<110>Si(001). Indeed, consistent with this crystal system, the ϕ scans of $\{202\}_{Si}$, $\{202\}_{BTO}$, and $\{202\}_{STO}$ in Fig. 1(b) also shows a 45° shift for the BTO and STO with respect to the Si peaks. Besides, the BTO crystal quality for both orientations is comparable. The full width half maximum of the $(002)_{BTO}$ rocking curve (ω-scan) is 0.8° and 0.7° for the a- and c-oriented BTO, respectively. Similarly, the RHEED patterns of both films, shown in Fig. 2(a), exhibit sharp streak-lines, revealing a good crystallinity of the BTO as well as a flat surface. This is in agreement with Fig. 2(b), which shows the transmission electron microscope (TEM) image for a-oriented BTO, illustrating low roughness on the top surface. However, we note that there is a 3.5 nm amorphous interfacial layer between the STO layer and the Si substrate. From the high-angle annular dark field scanning TEM (HAADF-STEM) image shown in Fig. 2(c), we can derive that this interfacial layer is actually composed of two layers. Since image contrast in HAADF-STEM is proportional to the atomic number squared (Z^2), the double layers at interface suggest layers with different compositions. From electron dispersion spectroscopy, the whole interfacial layer (IL) is found to be composed of a silicate compound with a graded distribution of Si, O, Sr, and Ti. The top layer contains more Sr and Ti, while the bottom layer is identified as being more SiO_x-rich. Such an amorphous double-layer interface is formed at the beginning of the STO preparation step. From our observations, a thicker STO brings about an increasing silicate thickness. Therefore, the IL of ~3.5 nm for c-oriented BTO (40-nm-thick STO buffer layer) is thicker than that of ~2.5 nm for a-oriented BTO (10-nm-thick STO buffer) [27]. Moreover, in agreement with Fig. 1(b), Fig. 2(c) indicates the epitaxial relationship between BTO, STO, and the Si(001) substrate, as labelled by the arrows overlaid on the picture. Despite the existence of the silicate IL, promising modulation bandwidth of 5 GHz [20], effective Pockels coefficient of 300 pm/V [21] and waveguide propagation loss of 6 dB/cm [28] have been successfully demonstrated.

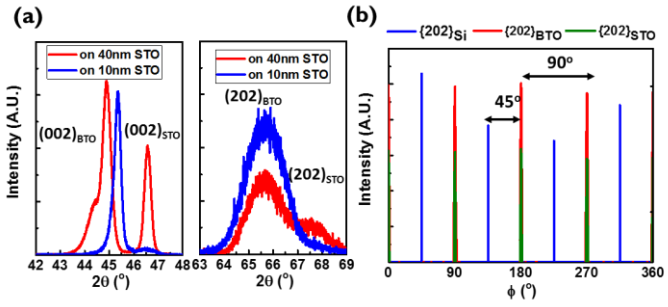

Fig. 1. (a) The ω-2θ XRD scans along $[001]_{BTO/STO}$ and $[101]_{BTO/STO}$ for a 100-nm-thick BTO layer on 10- and 40-nm-thick STO layer. (b) A ϕ-scan of $\{202\}_{Si}$, $\{202\}_{BTO}$, and $\{202\}_{STO}$ for 100-nm-thick BTO on a 40 nm STO layer.

Optical Materials EXPRESS

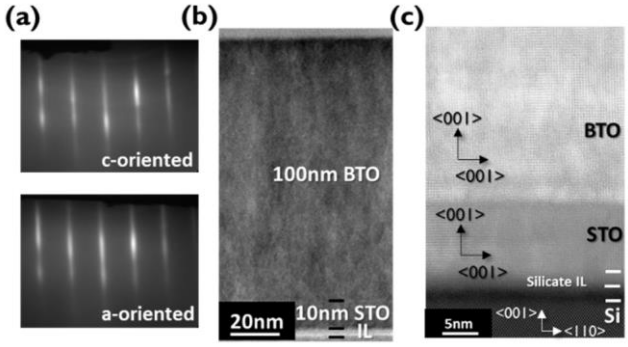

Fig. 2. (a) The RHEED patterns for c- and a-oriented BTO layers on Si(001). TEM (b) and HAADF-STEM (c) images for 100-nm-thick layers of a-oriented BTO on a Si(001) substrate with a 10-nm-thick STO buffer layer.

3.2 Electrical properties

During operation of the EO devices, the leakage current needs to be low to avoid deterioration of the applied field, limiting optical modulator performance. In this section, we focus on the a-oriented BTO sample and investigate the effect of post-process annealing on the leakage current. The annealing is carried out at different temperatures, under ambient oxygen exposure for 30 min. Then, we sputter a 10-nm-thick gold layer as a top electrode. The resulting current density versus voltage (J–V) curves are shown in Fig. 3(a). The corresponding current densities at + 1 V and –1 V are recorded in Fig. 3(b) and 3(c), respectively. The current density results using MBE in this work are within the range of those by pulsed laser deposition [29]. Given the ultra-high vacuum (UHV) epitaxial process, it is challenging to avoid the generation of oxygen vacancies in the as-grown samples, explaining the high leakage current above 100 mA/cm^2 at +/– 1 V [30]. According to the chemical equation:

$$O_o = v_o^{\cdot\cdot} + 2e^{/} + \tfrac{1}{2}O_2(g) \quad (1)$$

at oxygen sites (O_o) in the oxide, the creation of one oxygen vacancy with double positive charges ($v_o^{\cdot\cdot}$) will produce two free carriers ($e^{/}$) and one oxygen molecule (O_2). Therefore, in an oxygen-deficient condition, carriers created through oxygen vacancy formation cause the oxide to be conductive and absorptive in the near infrared-spectrum [31]. Although the as-deposited sample shows a high leakage current density, post-process annealing under ambient oxygen at increasing temperatures can suppress the leakage current dramatically. Following annealing at 600 °C for 30 min, the current density is reduced to 10^{-4} mA/cm^2 at +/– 1 V. In addition, such annealing process increases the silicate IL thickness from ~2.5 nm to ~5 nm, making the IL become more influential on the electrical phenomenon. The IL thickening enables the BTO/STO/silicate IL/p^+-Si heterostructure to behave more like an insulator. Therefore, after the oxygen annealing, the suppression of the current density at both bias polarities can result from the combinational effects of filling the oxygen vacancies and thickening the silicate IL [32]. Furthermore, ω-2θ XRD scans show that the BTO crystal structure does not noticeably change under such annealing process. Prior to EO characterizations, both the a- and c-oriented samples studied here are annealed at 600 °C for 30 minutes to improve electrical performance of the heterostructures.

Optical Materials EXPRESS

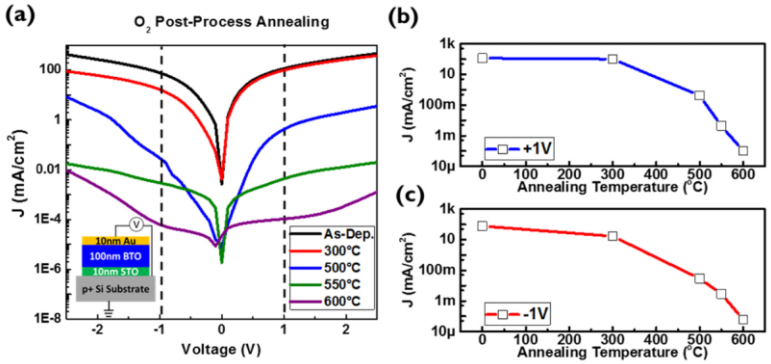

Fig. 3. (a) The J–V curves in terms of various post-process annealing temperatures under 30 min oxygen ambient for 100-nm-thick layers of a-oriented BTO on highly p-doped Si substrates with a 10 nm STO buffer layer. The top electrode is gold (10 nm). (b) and (c) are the current density at + 1 V and –1 V, respectively, for different annealing temperatures.

3.3 EO characterization using spectroscopic ellipsometry

In principle, spectroscopic ellipsometry (SE) measures the ratio of the reflection coefficients for the TE (r_{TE}) and TM (r_{TM}) polarized light waves that are incident on the stack under study. This ratio is then expressed as a function of the characteristic terms tan(Ψ) and Δ, as follows:

$$\frac{r_{TM}}{r_{TE}} = \tan(\Psi)e^{i\Delta} \tag{2}$$

Fitting an analytical model to the measured data then allows to extract the desired information (refractive index, thickness) of the different layers in the stack. Given that Δ cannot be related to a physical picture of the polarization ellipse in a straightforward manner, in practice one rather uses tan(Ψ) and cos(Δ) for presenting the results of an SE measurement. To enable efficient extraction of the BTO EO properties, we study its effect on the cos(Δ) spectrum in the following analysis.

To perform bias-dependent SE measurements, a transparent electrode must be prepared on the sample surface. The measured samples use a 200 nm indium tin oxide (ITO) layer as the top electrode and a highly p-doped Si substrate as the bottom electrode. In the remainder of this paragraph we use a 200 nm ITO/100 nm a-oriented BTO/10 nm STO/Si structure as an example to explain how the BTO index change induced by an applied voltage is derived. Figure 4(a) presents the cos(Δ) spectrum of this structure recorded with a signal acquisition time of 2 s and an applied voltage of 0 V at an angle of incidence (AOI) of 65°. The effect of applying a voltage on the measured cos(Δ) signal is then measured with a much longer acquisition time (90s) as certain discrete wavelengths (labelled by the red dots). Figure 4(b) shows the measured difference {cos(Δ(1V)) - cos(Δ(0V))}. As shown in the inset of Fig. 4(a) and in Fig. 4(b), the effect on cos(Δ) is small. If a standard parametric spectral fitting method were applied to extract the BTO EO response from such a minor difference in cos(Δ), unphysical results might be obtained, despite a high fitting quality [33]. Therefore, as an alternative, we used a numerical approach to determine the index change induced by applying a voltage over the BTO layer, based on the transfer matrix method (TMM).

Optical Materials EXPRESS

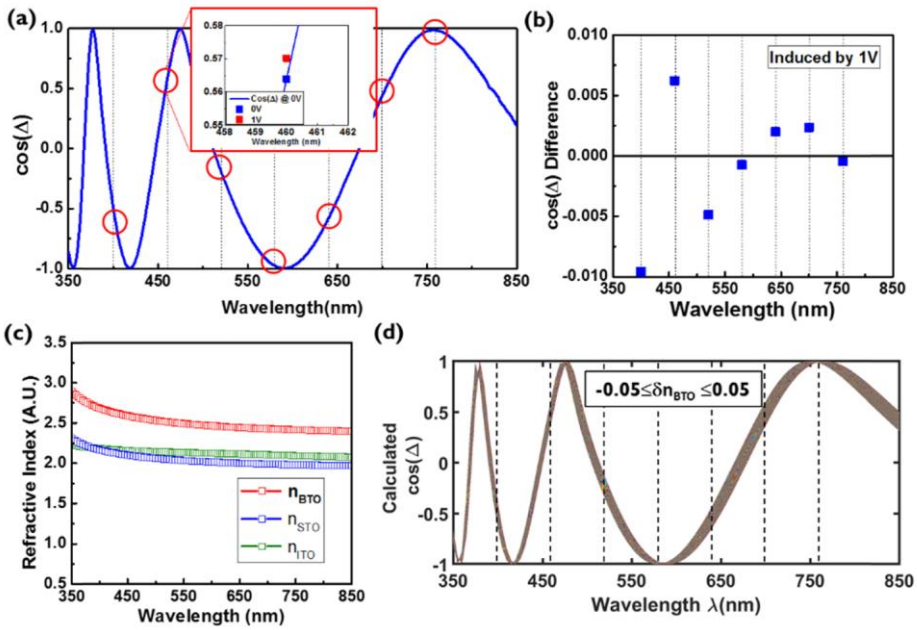

Fig. 4. (a) The measured cos(Δ) spectrum at AOI 65° for a-oriented BTO (100 nm) on a STO-buffered (10 nm) Si substrate at 0 V. The dotted lines indicate the wavelengths where the EO measurements with long acquisition time were executed. The inset shows an EO-induced spectrum shift at 460 nm. (b) The cos(Δ) difference induced by applying 1 V. (c) The refractive indices of BTO, STO, and ITO that are used in the spectrum calculation. (d) A simulated cos(Δ) curve using the TMM with a BTO index variation δn_{BTO} of between –0.05 and 0.05.

First, a standard parametric fitting procedure to a dispersion law expressed as a combination of a Tauc-Lorentz model and a Gauss function is used to extract the wavelength dependent refractive indices for BTO, STO and ITO. The optical effect of the few-nm-thick IL is negligible. The results are shown in Fig. 4(c). Then, based on Eq. (1), the expected cos(Δ) can be calculated using a TMM with known parameters, including the angle of incidence (AOI), and the thickness and optical indices of the ITO, BTO, STO and Si layers. Subsequently, we vary the BTO index around its measured value with δn_{BTO} changing from –0.05 to 0.05, to obtain different cos(Δ) spectra, thus simulating the effect of applying a voltage, as shown in Fig. 4(d). At each measured wavelength, Fig. 4(d) can then be used to derive the cos(Δ) difference over the range $0.05 \le \delta n_{BTO} \le 0.05$ with respect to the value at $\delta n_{BTO} = 0$. Finally, by comparing Fig. 4(b) with Fig. 4(d), the measured cos(Δ) difference can be translated in an associated δn_{BTO}. In the next section, the EO effect as measured in c-oriented and a-oriented BTO using the method described above will be discussed and compared.

Optical Materials EXPRESS

3.4 Comparison of the EO response for c-oriented and a-oriented BTO

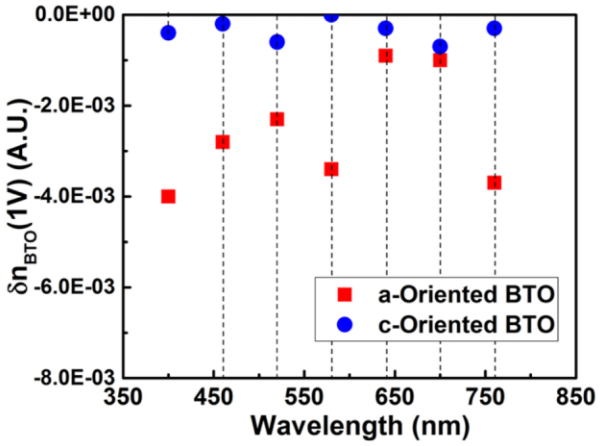

Fig. 5. δn_{BTO} at 1 V for a- and c-oriented BTO.

Figure 5 shows $\delta n_{BTO}(1\ V)$ for a-oriented and c-oriented BTO, calculated by the method described in the previous section. It can be clearly seen that the a-oriented BTO shows a larger δn_{BTO} than c-oriented BTO over the whole spectrum. To explain this, we consider single-domain c-oriented BTO, with its domain orientation (optical axis) along the z-axis, as shown in Fig. 6(a). Since BTO is an optically anisotropic material, its ordinary (n_o) and extraordinary indices (n_e) with respect to the crystal axes can be described through the index ellipsoid shown in Fig. 6(a) (without E-field). Then, the effect of applying an electric field is described by the associated deformation of the index ellipsoid according to:

$$(\frac{1}{n_o^2}+r_{13}E_z)x^2+(\frac{1}{n_o^2}+r_{13}E_z)y^2+(\frac{1}{n_e^2}+r_{33}E_z)z^2+2r_{51}E_y\mathrm{yz}+2r_{51}E_x\mathrm{xz}=1 \qquad (3)$$

with the Pockels tensor

$$r_{ij}=\begin{bmatrix}0 & 0 & r_{33}\\ 0 & 0 & r_{33}\\ 0 & 0 & r_{33}\\ 0 & r_{51} & 0\\ r_{51} & 0 & 0\\ 0 & 0 & 0\end{bmatrix}; \qquad (4)$$

the reported components r_{51} and r_{33} can be as large as 1300 and 105 pm/V for bulk BTO crystals, respectively [34]. Based on Eq. (3), the electric field should be applied perpendicular to the optical axis of the BTO, i.e. along the x- or y-axis, to exploit the strong r_{51} component of the Pockels tensor. Applying an electric field along the z-axis only exploits the much weaker r_{13} and r_{33} components, resulting in a weaker EO effect. Our samples have a top-down electrode configuration resulting in a vertical electric field as shown in Fig. 6(b). This explains why a stronger EO effect is measured in the a-oriented sample, where the optical axis is perpendicular to the electric field, than in the c-oriented sample, in which the electric field is parallel to the optical axis.

Optical Materials EXPRESS

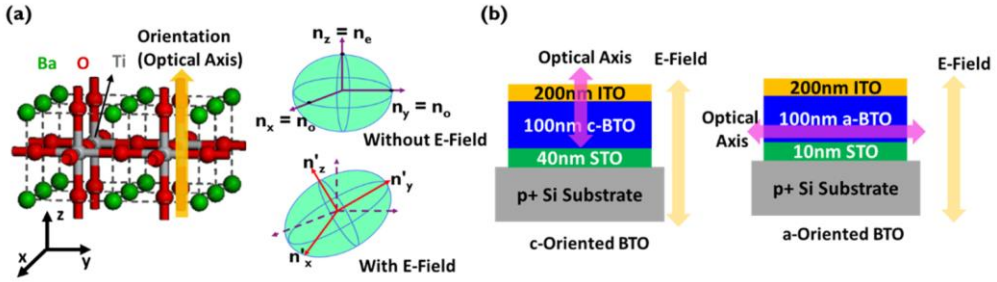

Fig. 6. (a) Lattice structure for c-oriented BTO and its index ellipsoid without and with an applied electric field. (b) Relationship between the electric field and the optical axis in c- and a-oriented BTO.

4. Conclusions

We prepared 100-nm-thick layers of c- and a-oriented BTO on Si(001) substrates with respectively 40 and 10 nm STO buffer layers. The orientation of the domains was identified by XRD and we utilize RHEED, TEM, and HAADF-STEM analysis to study the crystallinity of the grown BTO layers and the nature of the interface layer between the STO and Si substrate. Even though BTO shows good crystallinity, the UHV MBE process introduces many oxygen vacancies into the layer, resulting in large leakage currents. By post-process annealing in an oxygen ambient at 600 °C for 30 min, the leakage current is efficiently suppressed, ensuring a sufficient electric field can be built up in the BTO layer during device operation. Then, for both the c-oriented and the a-oriented BTO layers, we investigated how the domain structure influences the EO response, as measured by SE. Given the top-down electrode configuration, the a-oriented BTO layer shows a larger index difference δn_{BTO} compared with c-oriented BTO when an external bias of 1 V is applied. This is explained by the fact that the optical axis of a-oriented BTO is perpendicular to the applied electric field, allowing exploiting the strong r_{51} component in this case. The c-oriented BTO sample, however, which has its optical axis parallel to the electric field, shows a weaker EO response, because it relies on the smaller r_{13} and r_{33} components of the Pockels tensor. Therefore, this work provides not only a better understanding in how the domain orientation in a BTO thin film affects its EO response but also provides insights into how to design high performance BTO/Si hybrid modulators, taking into account the domain orientation of the BTO thin films grown on a Si(001) substrate.

Acknowledgments

This work was carried out as part of imec's industry affiliation program on Optical I/O. The authors thank imec's Material Component Analysis Department for material analysis, David Cheyns for constructive suggestions for EO analysis, and Hans Costermans and Kevin Dubois for the hardware support of our MBE system.